Solid-State Electronics 80 (2013) 124–134

Contents lists available at SciVerse ScienceDirect

Solid-State Electronics

journal homepage: www.elsevier.com/locate/sse

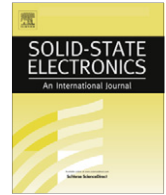

k.p based closed form energy band gap and transport electron effective mass model for [1 0 0] and [1 1 0] relaxed and strained Silicon nanowire

Ram Krishna Ghosh, Sitangshu Bhattacharya *, Santanu Mahapatra

Nano Scale Device Research Laboratory, Department of Electronic, Systems Engineering (formerly CEDT), Indian Institute of Science, Bangalore 560 012, India

ARTICLE INFO

Article history:
Received 15 March 2012
Received in revised form 27 October 2012
Accepted 5 November 2012

The review of this paper was arranged by S. Cristoloveanu

Keywords:
Silicon nanowire
Size quantization
Band gap
Effective mass
Strain

ABSTRACT

In this paper, we address a physics based closed form model for the energy band gap (E_g) and the transport electron effective mass in relaxed and strained [1 0 0] and [1 1 0] oriented rectangular Silicon Nanowire (SiNW). Our proposed analytical model along [1 0 0] and [1 1 0] directions are based on the **k.p** formalism of the conduction band energy dispersion relation through an appropriate rotation of the Hamiltonian of the electrons in the bulk crystal along [0 0 1] direction followed by the inclusion of a 4×4 Lüttinger Hamiltonian for the description of the valance band structure. Using this, we demonstrate the variation in E_g and the transport electron effective mass as function of the cross-sectional dimensions in a relaxed [1 0 0] and [1 1 0] oriented SiNW. The behaviour of these two parameters in [1 0 0] oriented SiNW has further been studied with the inclusion of a uniaxial strain along the transport direction and a biaxial strain, which is assumed to be decomposed from a hydrostatic deformation along [0 0 1] with the former one. In addition, the energy band gap and the effective mass of a strained [1 1 0] oriented SiNW has also been formulated. Using this, we compare our analytical model with that of the extracted data using the nearest neighbour empirical tight binding $sp^3d^5s^*$ method based simulations and has been found to agree well over a wide range of device dimensions and applied strain.

© 2012 Elsevier Ltd. All rights reserved.

1. Introduction

Emergence of Silicon Nanowires (SiNWs) as one-dimensional transistors has generated a challenging task to investig ate two of its fundamental band structure dependent electronic properties, one being the energy band gap (E_g) and the other being the electron effective mass along the carrier transport direction which drastically affects the carrier transport mechanism. However as the experimental study of these parameters at the nanoscale regime is extremely challenging, usually one relies on the atomic level simulations, the results of which are at par with the experimental observations.

In recent years, there has been an extensive study on the behaviour of E_g and the electron effective mass along different transport orientations in both relaxed and strained SiNWs by using ab initio and different empirical methods [1–5]. Albeit of these existing simulation results, there still lies a provocative challenge in developing an analytical solution of these electronic parameters due to the following reasons.

- enhanced electron mobility in relaxed and strained [1 0 0] and [1 1 0] channel Si [6],
- crossing of primed and unprimed subbands in SiNW when **k.p** formalism is used [3,4,7].
- closed form relation of E_g and electron effective mass in the presence of strain, and
- standardizing energy parameters in TCAD software for applications in nanodevices [8].

In this work we use a degenerate **k.p** theory in a relaxed bulk Si crystal to obtain the conduction band dispersion relation and quantized subband energies at the Γ and off-Γ axes in a [1 0 0] oriented SiNW together with 4×4 Lüttinger Hamiltonian dispersion relation of heavy holes (HHs) and light holes (LHs) subbands. This is followed by an appropriate rotation of the conduction band and valence band Hamiltonian to explain the corresponding dispersion relation and subband energies at both the axes of a [1 1 0] oriented SiNW. By including the quantum confinement effects, we next formulate the direct and indirect energy band gap and the transport electron effective masses considering both the channel orientations. In case of [1 0 0] SiNW, we have studied the effect of a uniaxial and a biaxial strain on the E_g and the transport electron effective mass. The uniaxial strain has been applied along the [1 0 0] direction while the biaxial strain consists of a hydrostatic deformation strain along [0 0 1] together with the same uniaxial one. The effect

* Corresponding author.
E-mail addresses: ramki.phys@gmail.com (R.K. Ghosh), isbsin@yahoo.co.in (S. Bhattacharya), santanu@cedt.iisc.ernet.in (S. Mahapatra).

0038-1101/$ - see front matter © 2012 Elsevier Ltd. All rights reserved.
http://dx.doi.org/10.1016/j.sse.2012.11.001

of these strains together with a shear strain on the variation of transport electron effective mass in a [1 1 0] oriented SiNW has further been investigated. In this case, the uniaxial strain is along [1 1 0] direction while the biaxial part contains the same hydrostatic one together with the [1 1 0] uniaxial. Both the tensile and compressive strain is being associated with this uniaxial and biaxial strain to investigate the variation of these two parameters. We have formulated the energy band gap and effective electron mass in a (0 0 1) wafer along [1 0 0] and [1 1 0] channel directions, which can also be extended for (0 0 1)/[1 1 1] case, as this is preferable to control the carrier mobility both in the absence and presence of strain. The analytical results of the band gap and the electron transport effective masses in both relaxed and strained rectangular SiNW along the former two channel orientations are further being compared with the data extracted from the Atomistix ToolKit (ATK) [9] which uses a nearest neighbour empirical tight binding $sp^3d^5s^*$ method. Our analytical model stands valid for the cases where the strain is within 1% and the spin–orbit coupling does not influence the conduction energy band.

2. Model and discussions

2.1. Importance of **k.p** approach over EMA

The importance of **k.p** method over EMA in the proper description of the energy band structure of Si lies in the fact that the non-degenerate EMA equation used for [0 0 1] valleys fails to describe the conduction band wrapping and the subband structure correctly in (1 1 0) oriented Si films [6,10]. In particular, to correlate a complete analytical conduction band dispersion relation with the advanced empirical tight binding model like $sp^3d^5s^*$, a two band degenerate **k.p** model should be used where a second conduction band close to the first conduction band must be taken into account, the two of which becomes degenerate just at the *X* point [10]. These are generally called as primed and unprimed bands respectively. This phenomenon is however not arrested in the simple non-parabolic EMA analyses [4]. Further the EMA also neglects any change in the nature of the energy band gap with the application of strain properly [7].

2.2. Relaxed [1 0 0] SiNW

Intrinsic relaxed bulk Si crystal consists of six equivalent conduction band minima located symmetrically along ⟨1 0 0⟩ at a distance of approximately $k_0 = 0.15\left(\frac{2\pi}{a_0}\right)$ from the *X* point along Γ direction in a three dimensional Brillioun zone, in which a_0 is the relaxed lattice constant of Si. The electron energy dispersion relation using this two band degenerate **k.p** model for relaxed bulk Si crystal along [0 0 1] transport direction can be written as [10,11]

$$E_{\pm}(k) = \frac{\hbar^2 k_x^2}{2m_{1_\pm}} + \frac{\hbar^2 k_y^2}{2m_{2_\pm}} + \frac{\hbar^2 (k_z + k_{min})^2}{2m_{3_\pm}} \pm \sqrt{\left(\frac{\hbar}{m_0}k_z p\right)^2 + \left(\frac{\hbar^2 k_x k_y}{M_\pm}\right)^2} \quad (1)$$

in which *E* is the electron energy as measured from the bottom of the conduction band minimum, ± represents the primed and unprimed band (± at the subscript of the effective masses represents their corresponding values at the primed and unprimed valleys), the momentum matrix element identity [10,11] is $\frac{p}{m_0} = \frac{\hbar_0}{m_{3_\pm}}$, $\frac{1}{M_\pm} \approx \frac{1}{m_{1_\pm}} - \frac{1}{m_0}$. In case of unprimed band the effective masses are $m_{1_-} = m_t, m_{2_-} = m_t$ $m_{3_-} = m_l$ and for the primed band the effective masses are $m_{1_+} = m_l, m_{2_+} = m_t, m_{3_+} = m_t$ where m_l(=0.91m_0) and m_t(=0.19m_0) are the longitudinal and transverse electron effective mass [2] in which m_0 is the free electron mass, $\hbar = \frac{h}{2\pi}, h$ is the Planck's constant and k_x, k_y and k_z are the electron wave vectors along *x*, *y* and *z* direction respectively. Neglecting the spin–orbit interaction between the HH and LH with split-off holes, the hole dispersion relation at the Γ point can be written as [12]

$$E = Ak^2 \pm \left[B^2k^4 + C^2\left(k_x^2k_y^2 + k_y^2k_z^2 + k_z^2k_x^2\right)\right]^{1/2} \quad (2)$$

where in this case, *E* is the hole energy as measured from the top of the valance band maxima, ± indicates the HH and LH bands, $k^2 = k_x^2 + k_y^2 + k_z^2$ and $A = -(4.1 \pm 0.2)(\hbar^2/2m_0)$, $|B| = (1.6 \pm 0.2)(\hbar^2/2m_0)$ and $|C| = (3.3 \pm 0.5)(\hbar^2/2m_0)$ are the inverse mass band parameters [12]. It appears that due to the occurrence of the square root in Eq. (2), the HH and LH dispersion relation in general cannot be described by the effective masses [10]. Keeping this in view, we assume that the Lüttinger parameters *A*, *B* and *C* are independent of the cross-sectional dimensions.

The energy band structure of SiNW whose electron transport is along [1 0 0] direction is an involved task. The symmetry between the six equivalent conduction band minima is now displaced due to the difference in the effective masses as a result of the quantum confinement of the carriers along the two lateral directions as also conveyed through the earlier investigations done with the $sp^3d^5s^*$ simulation method [1,2,13]. Because of this, the six conduction band valleys are now grouped in a fourfold degenerate bands (Δ_4) at Γ-axis and twofold degenerate bands (Δ_2) at off-Γ at a distance of about $k_{x_{min}} \approx \pm 0.37\frac{\pi}{a_0}$ from the Γ-axis [13]. Due to the higher quantized electron effective mass in the Δ_4 valley along the quantized directions, the corresponding energy minimum is at a lower position than that of the Δ_2 valley, thus making the SiNW to be a direct band gap. With an increase in the SiNW cross-section, this quantized effective mass converges to its respective bulk value and the energy wave vector minimum tends to an indirect band gap [3]. Thus in [1 0 0] SiNW structure, the energy band gap depends not only on the effective masses at the band minima but also onto the subband energies along the confinement directions.

The [1 0 0] SiNW band structure diagram has been evaluated using the ATK simulator and is shown in Fig. 1. Fig. 1a exhibits the Si atomic configuration of a cleaved [1 0 0] with sp^3 passivated Hydrogen atoms. This has been done to remove the surface states in the band gap region due to dangling Si bonds on the surface of the nanowire. In this configuration we have considered the nearest Si–Si and Si–H bond lengths to be 0.235 nm and 0.152 nm respectively. The calculation of the energy band structure is done by nearest neighbour $sp^3d^5s^*$ tight binding method. In this method, each atomic lattice of the configuration is considered by a $sp^3d^5s^*$ basis and the spin–orbit interaction among them is ignored. In addition, the *k*-point samplings of $1 \times 1 \times 21$ grid were used with mesh cut-off energy of 10 Hartree. The energy band structure of a 1.25 nm cross-sectional dimension of a [1 0 0] oriented SiNW has been shown in Fig. 1b which clearly exhibits that the energy band gap is a direct one at the Γ axis while the off-Γ valleys exhibits an indirect energy band gap, a value higher that the former one, as already known from the existing studies [2,13]. Further, we notice that the valley splitting even at room temperature at Γ and off-Γ axis is significantly less. It should be noted that one may ignore the importance of the valley splitting for the present analyses of the determination of the band gap and transport effective electron mass. By this, we mean that it is the lowest conduction splitted valley and highest valance splitted valley which determines the gap and the transport electron effective mass for that valley. Although the valley splitting is extremely important for analysing mobility, electrical resistance, etc. which incorporates the total number of subbands and channels, however for the determination of energy

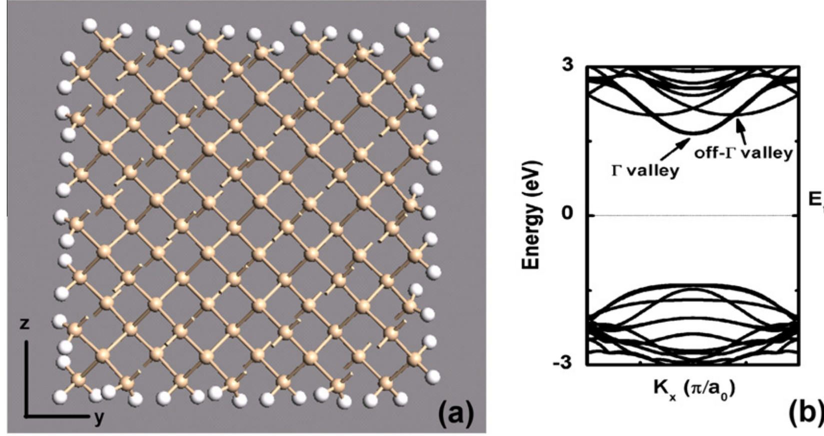

Fig. 1. (a) ATK built sp[3] hydrogen passivated (100) SiNW plane of a [100] oriented channel of SiNW with cross-sectional thicknesses d_y and d_z along y and z directions respectively and (b) energy band structure of [100] Hydrogen passivated SiNW of $1.25 \times 1.25\ \text{nm}^2$ cross-sectional area using ATK builder which uses a nearest neighbour empirical tight binding sp[3]d[5]s* method.

band gap and the effective mass at the lowest valley one may ignore the next higher valley together with the interaction between the two.

Analytically, the band structure of relaxed SiNW at Γ and off-Γ axis along the [100] transport direction can be written by rotating the Hamiltonian of [001] direction as

$$E_{\pm}(k) = \frac{\hbar^2 (k_x + k_{min})^2}{2m_{3_\pm}} + \frac{\hbar^2}{2m_{2_\pm}}\left(\frac{\pi}{d_y}\right)^2 + \frac{\hbar^2}{2m_{1_\pm}}\left(\frac{\pi}{d_z}\right)^2 \pm \sqrt{\left(\frac{\hbar^2 k_0 k_x}{m_{3_\pm}}\right)^2 + \left(\frac{\hbar^2}{M_\pm}\left(\frac{\pi}{d_z}\right)\left(\frac{\pi}{d_y}\right)\right)^2} \quad (3)$$

Eq. (3) is the result of the assumption that the carriers obey the periodic Bloch waves together with the van-Hove singularity conditions occurring due to the carrier confinement along the k_x and k_y directions. At this point it should be noted that although, the subband energies of the two band **k.p** model cannot simply be obtained from the "particle-in-a-box" formalism [14] however, to achieve a simplistic closed form analysis considering a small coupling between the bands [10] rather than the rigorous numerical based approach, we consider the "particle-in-a-box" formalism. Nevertheless, it should also be emphasised that in order to estimate the electronic properties of nonlinear energy bands under the two band or three band Kane's type model, this approach is useful, (for example see [11,15–18]). Under such "particle-in-a-box" conditions, we have used the electron wave vectors to be $k_y = \left(\frac{n_y \pi}{d_y}\right)$ and $k_z = \left(\frac{n_z \pi}{d_z}\right)$, it is customary that we use $n_y = 1$ and $n_y = 1$ for describing the lowest quantized wave vectors along the respective transformed directions.

The use of Eq. (3) then leads to the lowest subband quantized energies at both the valleys as

$$E_{1,1_\pm}(k) = \frac{\hbar^2 k_{x_{min}}^2}{2m_{3_\pm}} + \frac{\hbar^2}{2m_{2_\pm}}\left(\frac{\pi}{d_y}\right)^2 + \frac{\hbar^2}{2m_{1_\pm}}\left(\frac{\pi}{d_z}\right)^2 \pm \sqrt{\left(\frac{\hbar^2}{M_\pm}\left(\frac{\pi}{d_z}\right)\left(\frac{\pi}{d_y}\right)\right)^2} \quad (4)$$

In which $k_{x_{min}} = 0$ and $\pm 0.37\frac{\pi}{a_0}$ at Γ and off-Γ valley respectively.

Assuming that the holes obey the same "particle-in-a-box" formalism, Eq. (2) leads to the ground state valance subband maxima structure at the Γ-axis as

$$E^{v}_{\pm}(k) = A\left[\left(\frac{\pi}{d_y}\right)^2 + \left(\frac{\pi}{d_z}\right)^2\right] \pm \sqrt{B^2\left[\left(\frac{\pi}{d_y}\right)^2 + \left(\frac{\pi}{d_z}\right)^2\right]^2 + C^2\left(\left(\frac{\pi}{d_y}\right)^2\left(\frac{\pi}{d_z}\right)^2\right)} \quad (5)$$

Thus using Eqs. (4) and (5), the direct and indirect energy band gap at Γ and off-Γ axis in the relaxed SiNW can be written respectively as

$$E^{Direct}_{g_{NW}} = E_g + E_{1,1_-} + |E^v_+| \quad (6)$$

and

$$E^{Indirect}_{g_{NW}} = E_g + E_{1,1_+} + |E^v_+| \quad (7)$$

where E_g(=1.12 eV) is the bulk value of the indirect band gap. It appears from Eqs. (6) and (7) that the band gap in the two confined valleys at Γ and off-Γ depends on the corresponding quantum numbers n_y and n_z. However, it should be noted that, physically the energy band gap of 1D nanowire is the absolute energy difference between the lowest conduction subband and top most valance subband level respectively.

Fig. 2 shows the variation of both the Γ and off-Γ axis band gap in [100] oriented relaxed SiNW as function of the cross-sectional dimension of equal thickness. It appears that as the thickness increases, the effect of the quantum confinement on both the valleys of the conduction subband and valence subband respectively plays a crucial role in determining the magnitude of the energy band gap. This can be understood as follows:

With the increase in the cross-sectional dimension the band gap at both Γ and off-Γ axis decreases, however at a different rate due to the difference in the effective masses in the respective valleys. As the thickness increases above 4 nm, it is the band gap at Γ axis that converges to 1.12 eV, which is essentially the difference between the conduction band minima and valance band maxima at the Γ axis, where the bulk conduction band minima at k_0 comes implicitly in the degenerate band formulation. The off-Γ axis band gap attains a value of 1.55 eV, a value higher than that of the former due to the presence of the non-zero factor in Eq. (4) as seen from the Brillioun zone boundary which makes $E_{1,1_+}$ to attain a saturation value of 0.49 eV. However, if it is considered as the origin of the minimum of the valley, then $E_{1,1_+}$ converges to 0 eV and we get the bulk result.

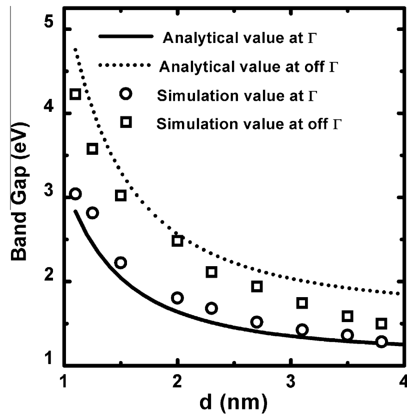

Fig. 2. Plot of the direct and indirect energy band gap using Eqs. (6) and (7) in relaxed [1 0 0] SiNW as function of lateral wire-width $d_y = d_z = d$. The symbols are our extracted simulation data which has been obtained by using the ATK by passivating the Si atoms at the surface of the wire using Hydrogen atoms as shown in Fig. 1 (b) followed by the use of a nearest neighbour empirical tight binding $sp^3d^5s^*$ method.

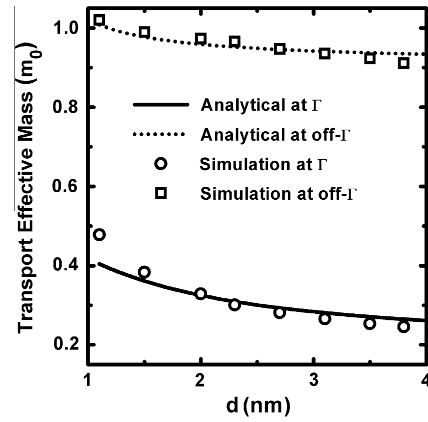

Fig. 3. Plot of the transport effective electron mass at the minima of the Γ and off-Γ subband valleys using Eqs. (8) and (9) as function of wire thickness. The symbol represents the extracted data from the energy band structure obtained using ATK simulation.

The effect of the carrier confinement leads to the discrete subband energy levels for both the electrons and holes. In case of valance bands, the HH and LH forms separate energy subband levels due to the difference in their energy. Thus using this, it appears that the first subband of E_+^v for HH in a 1.5 × 1.5 nm^2 SiNW is about 0.7 eV below compared to that of the maxima point of the HH in case of bulk. However for the LH subband, E_-^v is about 2.7 eV below the same. Thus, we see that the energy band gap difference in case of SiNW should be considered from the lowest conduction subband to the lowest HH subband, which is precisely meant by Eqs. (6) and (7).

The electron effective mass along [1 0 0] direction in both the valleys can then be written as

$$m_{x_-} = m_{1_-}\left(1+\frac{\sqrt{\sigma_-}}{\sqrt{E_{g_{NW}}^{Direct}+\sigma_- - 2\phi_-}}\right) \tag{8}$$

and

$$m_{x_+} = m_{1_+}\left(1+\frac{\sqrt{\sigma_+}}{\sqrt{E_{g_{NW}}^{Indirect}+\sigma_+ - 2\phi_+}}\right) \tag{9}$$

in which $\sigma_\pm = \frac{\hbar^2 m_{1_\pm}}{M_\pm^2}\left(\frac{\pi}{d_y}\right)^2$ and $\phi_\pm = \frac{\hbar^2}{2m_{2_\pm}}\left(\frac{\pi}{d_y}\right)^2$.

Fig. 3 exhibits the variation of the transport effective mass along [1 0 0] direction in relaxed SiNW as a function of the cross sectional dimension. In case of the lowest Δ_4 subband at Γ, the transport effective mass decreases and converges to its bulk value 0.19 m_0 with the increase in the wire-width, thus confirming the result that electrons in lowest subband carries a lighter transport effective mass. In case of the lowest (Δ_2) subband at off-Γ, the transport effective mass decreases and converges to the bulk value 0.91 m_0. Using this approach, we observe that our analytical model for both the energy band gap and transport effective mass in both the valleys agrees well with the extracted data from the $sp^3d^5s^*$ model and exhibits a good trend as also depicted elsewhere [2,5]. The slight inconsistencies between the data and our analytical model might be due to the complete negligence of the spin–orbit interaction between the split-off holes and HH/LH in our model. The other part of the error comes due to the omission of the interaction of the plane waves of Hydrogen on the Si-atoms due to which the band structure of ultra-small thin SiNW gets affected.

2.3. Relaxed [1 1 0] SiNW

In case of relaxed [1 1 0] SiNW, the six conduction band valleys are now grouped in Δ_2 at Γ-axis and Δ_4 at off-Γ at a distance of about $K_{x_{min}} \approx \pm 0.19\frac{\pi}{a_0}$ from the first Brillioun zone boundary [13]. The higher quantized electron effective mass in the Δ_2 valley along the quantized directions leads to a corresponding energy minimum at a lower position than that of the Δ_4 valley and making the SiNW to be a direct band gap which is diametrically opposite with respect to the [1 0 0] oriented case. The [1 1 0] SiNW band structure simulation has been evaluated using the ATK simulator using the aforementioned similar procedure and is shown in Fig. 4a. The energy band structure of a 1.25 nm cross-sectional dimension of a [1 1 0] oriented SiNW has been shown in Fig. 4b which clearly exhibits that the energy band gap is a direct one at the Γ axis while the off-Γ valley exhibits an indirect energy band gap. Further, we see a sharp valley splitting both at Γ and off-Γ axis. This splitting energy at both the axes is however largest for same cross-sectional dimensions as compared with other channel orientation like [1 0 0] and [1 1 1] [2]. It can be seen that in our present case for 1.25 nm that this splitting energy at Γ axis is about 470 meV while at the off-Γ axis this is about 91 meV.

Analytically, the band structure of relaxed SiNW in the [1 1 0] coordinate frame of reference can be obtained by appropriately rotating the bulk Hamiltonian following [19] for each pair of the valleys. This leads to the off-Γ axis electron energy dispersion relation of the lowest subband, as measured from the Brillioun zone boundary as

$$E(K) = \frac{\hbar^2(K_x+K_{x_{min}})^2}{2m_{1_4}} + \frac{\hbar^2}{2m_{2_4}}\left(\frac{\pi}{d_y}\right)^2 + \frac{\hbar^2}{2m_{3_4}}\left(\frac{\pi}{d_z}\right)^2 + \frac{\hbar^2(K_x+K_{x_{min}})}{2m_{s_4}}\left(\frac{\pi}{d_y}\right) + \sqrt{\left(\frac{\hbar^2 k_0}{m_{3_+}}\left(\frac{\pi}{d_z}\right)\right)^2 + \left(\frac{\hbar^2\left((K_x+K_{x_{min}})^2 - \left(\frac{\pi}{d_y}\right)^2\right)}{2M_4}\right)^2} \tag{10}$$

in which $m_{1_4} = m_{2_4} = \frac{2m_{1_+}m_{2_+}}{m_{1_+}+m_{2_+}}$, $m_{3_4} = m_{3_+}$, $m_{s_4}^{-1} = m_{1_+}^{-1} - m_{2_+}^{-1}$ and $M_4^{-1} = m_{1_+}^{-1} - m_0^{-1}$ for transport along [1 1 0] direction where, it should be noted that in case of thin (1 1 0) oriented Si films, m_t in $M^{-1} = m_t^{-1} - m_0^{-1}$ is the transport effective mass [10]. Eq. (10) is

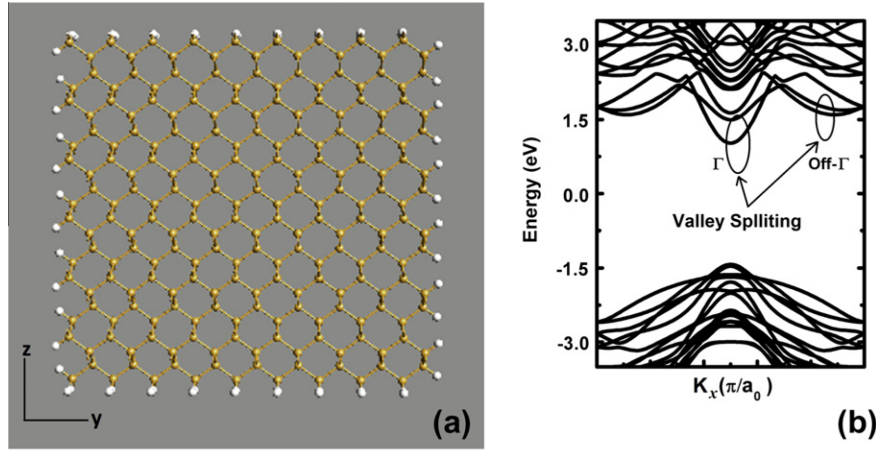

Fig. 4. (a) ATK built sp^3 Hydrogen passivated (1 1 0) SiNW plane of a [1 1 0] oriented channel of SiNW and (b) Energy band structure of [1 1 0] SiNW of 1.25 × 1.25 nm^2 cross-sectional area using sp^{3}d^{5}s* method.

the result of the same earlier assumption that the carriers obey the periodic Bloch waves together with the van-Hove singularity conditions occurring due to the carrier confinement along the transformed K_y and K_z directions.

The use of Eq. (10) then leads to the lowest subband quantized energy at the off-Γ valley as

$$E_{1,1_4} = \frac{\hbar^2 K_{x_{min}}^2}{2m_{1_4}} + \frac{\hbar^2}{2m_{2_4}}\left(\frac{\pi}{d_y}\right)^2 + \frac{\hbar^2}{2m_{3_4}}\left(\frac{\pi}{d_z}\right)^2 + \frac{\hbar^2 K_{x_{min}}}{2m_{s_4}}\left(\frac{\pi}{d_y}\right) + \sqrt{\left(\frac{\hbar^2 k_0}{m_{3_+}}\left(\frac{\pi}{d_z}\right)\right)^2 + \left(\frac{\hbar^2\left(K_{x_{min}}^2 - \left(\frac{\pi}{d_y}\right)^2\right)}{2M_4}\right)^2} \quad (11)$$

The expression for the energy dispersion relation for the twofold conduction subbands at Γ for [1 1 0] SiNW can be written as

$$E(K) = \frac{\hbar^2 (K_x + K_{x_{min}})^2}{2m_{1_2}} + \frac{\hbar^2}{2m_{2_2}}\left(\frac{\pi}{d_y}\right)^2 + \frac{\hbar^2}{2m_{3_2}}\left(\frac{\pi}{d_z}\right)^2 - \sqrt{\left(\frac{\hbar^2 k_0}{m_{3_-}}\left(\frac{\pi}{d_z}\right)\right)^2 + \left(\frac{\hbar^2\left((K_x + K_{x_{min}})^2 - \left(\frac{\pi}{d_y}\right)^2\right)}{2M_2}\right)^2} \quad (12)$$

in which $m_{1_2} = m_{2_2} = \frac{2m_{1_-}m_{2_-}}{m_{1_-}+m_{2_-}} = m_t$, $m_{3_2} = m_{3_-} = m_l$ and $M_2^{-1} = m_{1_-}^{-1} - m_0^{-1}$ for transport along [1 1 0] direction. Eq. (12) leads to the lowest subband energy at Γ axis ($K_{x_{min}} = 0$) as

$$E_{1,1_2} = \frac{\hbar^2}{2m_{2_2}}\left(\frac{\pi}{d_y}\right)^2 + \frac{\hbar^2}{2m_{3_2}}\left(\frac{\pi}{d_z}\right)^2 - \sqrt{\left(\frac{\hbar^2 k_0}{m_{3_-}}\left(\frac{\pi}{d_z}\right)\right)^2 + \left(\frac{\hbar^2\left(\frac{\pi}{d_y}\right)^2}{2M_2}\right)^2} \quad (13)$$

The bulk energy dispersion relation for HH and LH using the transformed [1 1 0] axis can respectively be written as

$$E(K) = AK^2 \pm \sqrt{B^2K^4 + C^2\left(\frac{1}{4}\left(K_x^2 - K_y^2\right) + K_z^2\left(K_x^2 + K_y^2\right)\right)^2} \quad (14)$$

Thus, Eq. (14) leads to the valance subband maxima structure at the Γ-axis as

$$E_{\pm}^{v} = A\left[\left(\frac{\pi}{d_y}\right)^2 + \left(\frac{\pi}{d_z}\right)^2\right] \pm \sqrt{B^2\left[\left(\frac{\pi}{d_y}\right)^2 + \left(\frac{\pi}{d_z}\right)^2\right]^2 + C^2\left(\frac{1}{4}\left(\frac{\pi}{d_y}\right)^4 + \left(\frac{\pi}{d_y}\right)^2\left(\frac{\pi}{d_z}\right)^2\right)} \quad (15)$$

Hence using Eqs. (13) and (15), the direct energy band gap at Γ for the relaxed [1 1 0] SiNW can be written as

$$E_{g_{NW}}^{Direct} = E_g + E_{1,1_2} + |E_+^v| \quad (16)$$

and using the Eqs. (11) and (15), the indirect energy band gap at off-Γ will be

$$E_{g_{NW}}^{Indirect} = E_g + E_{1,1_4} + |E_+^v| \quad (17)$$

Fig. 5a shows the variation of both the Γ and off-Γ axis band gap for [1 1 0] oriented relaxed SiNW as function of the cross-sectional dimension of equal thickness. With the increase in the cross-sectional dimension, both the direct and indirect band gap follows the same nature of decrement as exhibited in Fig. 2 of [1 0 0] oriented SiNW, however at a different rate due to the difference in the effective masses in the respective valleys. As the thickness increases, it is the band gap at Γ axis that converges to 1.12 eV. The off-Γ axis band gap attains a value of 1.19 eV, a value higher than that of the former due to the presence of the non-zero factor in Eq. (11) as seen from the Brillioun zone boundary which makes to attain a saturation value of 0.07 eV. However, if it is considered as the origin of the minimum of the valley, then $E_{1,1_4}$ converges to 0 eV and we get the bulk result. Comparing Fig. 2 and Fig. 5a we see that the band gap of [1 0 0] oriented SiNW is larger than that of the corresponding [1 1 0] one for the respective valleys as also similarly exhibited elsewhere [3,13].

The electron effective mass along [1 1 0] direction can then be defined in the two valleys as

$$m_{x_2} = \frac{m_{1_2}}{1 + \left(\left(\frac{\hbar^2 m_{1_2}}{2M_2^2}\right)\left(\frac{\pi}{d_y}\right)^2\left[\left(\frac{\hbar^2 k_0}{m_{3_-}}\left(\frac{\pi}{d_z}\right)\right)^2 + \left(\frac{\hbar^2}{2M_2}\left(\frac{\pi}{d_y}\right)^2\right)^2\right]^{-\frac{1}{2}}\right)} \quad (18)$$

and

$$m_{x_4} = \frac{m_{1_4}}{\left\{1 + \frac{\hbar^2}{2M_4^2}\xi\right\}} \quad (19)$$

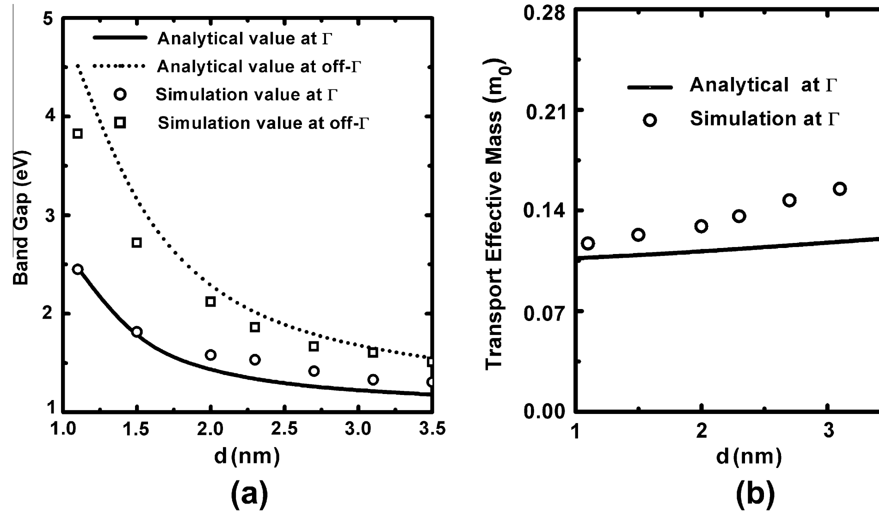

Fig. 5. (a) Plot of the direct and indirect energy band gap using Eqs. (16) and (17) in relaxed [1 1 0] SiNW as function of lateral wire-width $d_y = d_z = d$. The symbols are our extracted simulation data which has been obtained by using nearest neighbour empirical tight binding sp^{3}d^{5}s* method. (b) Plot of the transport effective electron mass at the minima of the Γ subband valley using Eq. (18) as function of wire thickness. The symbol represents the extracted data from the energy band structure obtained using ATK simulation.

for Γ and off-Γ valleys in which

$$\xi = \frac{1}{\sqrt{\zeta}}\left\{3K_{x_{min}}^2 - \left(\frac{\pi}{d_y}\right)^2 - \frac{1}{2\zeta}\left(\frac{\hbar^2 K_{x_{min}}}{M_4}\right)^2\left(K_{x_{min}}^2 - \left(\frac{\pi}{d_y}\right)^2\right)^2\right\} \text{ where}$$

$$\zeta = \left[\left(\frac{\hbar^2 k_0}{m_{3_+}}\left(\frac{\pi}{d_z}\right)\right)^2 + \left(\frac{\hbar^2}{2M_4}\left(K_{x_{min}}^2 - \left(\frac{\pi}{d_y}\right)^2\right)\right)^2\right].$$

Fig. 5b exhibits the variation of the transport effective mass of the relaxed SiNW as a function of the cross sectional dimension. In case of the lowest subband at Γ, the transport effective mass increases and converges to its bulk value 0.19 m_0 with the increase in the wire-width. This is opposite to the behaviour arrested in the case of [1 0 0] oriented SiNW.

2.4. Effect of cross-sectional shape

The analytical model as developed in this work for both the rectangular channel orientations can also be compared to the results of the band gap of a circular SiNW under identical conditions [4,20]. It should be noted that by fixing the reference frame to the square cross-sectional SiNW (at 1 nm^2, [20]), the maximum separation in the energy scale of the energy band gap between the square cross-sectional SiNW and circular cross-sectional SiNW is less than 6%, if varied with cross-sectional dimension. However, if varied with cross-sectional area, the separation is less than 1% ([4]). The separation of the energy band gap between the square cross-sectional SiNW and triangular cross-sectional SiNW is less than 38% (at 1 nm^2, [20]), while if plotted with area, the separation lies within 1% (at 1 nm^2, [20]). The deviation between the effective mass in square cross-sectional SiNW from that of circular is less than 1% ([4], if varied with cross-sectional area). For triangular case, this deviation is 22% ([20], if varied with cross-sectional area).

2.5. Strained [1 0 0] SiNW

Strain effects in bulk Si crystal along different directions have been extensively studied in past few decades [21,22]. Recently using the density functional theory, the effect of both uniaxial and biaxial strain on the band structure of a [1 0 0] oriented SiNW has been shown, where the modification of the positions of already lifted Δ_4 and Δ_2 valleys due to the quantum confinement effects has been considered [23]. This splitting of the valleys in relaxed SiNW however is not arrested by EMA approach [4]. For our present quantitative analysis, we take into consideration of a uniaxial and hydrostatic strain along [1 0 0] and [0 0 1] directions respectively. Fig. 6 schematically exhibits this situation on the conduction and valance bands for both tensile (Fig. 6a) and compressive (Fig. 6b) strains on a [1 0 0] oriented SiNW. In case of a SiNW, an application of a tensile hydrostatic strain shifts up the average energy of the conduction band with respect to its six equivalent valleys. In addition, a uniaxial strain along [1 0 0] splits this conduction band into Δ_2 and Δ_4. The position of these valleys about their bulk relaxed value however, strictly depends whether the strain is tensile or compressive. As shown in Fig. 6a the average energy of these set of subbands under the tensile hydrostatic strain along [0 0 1] shifts up by the same amount. However, the presence of a uniaxial compressive strain along [1 0 0] direction makes Δ_4 to be higher in energy than that of Δ_2 [23] as shown in Fig. 6b. In case of valance bands, the HH and LH split as subband energy levels (Eq. (5)) in which a tensile hydrostatic strain shifts up their respective average position, while a uniaxial tensile strain shifts up the HH subbands over LH subbands (Fig. 6a).

We now discuss a quantitative analysis of the energy band gap and transport electron effective masses under the presence of a biaxial strained [1 0 0] SiNW based on the degenerate **k.p** formalism as stated earlier. Further, in case of the splitted valance bands, we assume that the average position of the HH and LH subband almost coincides with the HH subband due to the higher effective mass of the former. The appropriate electron energy dispersion relation for strained bulk Si crystal along [1 0 0] transport can be extended following [10] as

$$E_{\pm}^{\varepsilon}(k) = \frac{\hbar^2(k_x + k_{min})^2}{2m_{3_\pm}} + \frac{\hbar^2}{2m_{2_\pm}}\left(\frac{\pi}{d_y}\right)^2 + \frac{\hbar^2}{2m_{1_\pm}}\left(\frac{\pi}{d_z}\right)^2 \pm \left\{\delta E_c + \sqrt{\left(\frac{\hbar^2 k_0 k_x}{m_{3_\pm}}\right)^2 + \left(\frac{\hbar^2}{M_\pm}\left(\frac{\pi}{d_z}\right)\left(\frac{\pi}{d_y}\right)\right)^2}\right\} \quad (20)$$

in which $\delta E_c = D_d(\varepsilon_{zz} + \varepsilon_{xx}) + D_u\varepsilon_{xx}$ is the strain induced shift of the conduction band, $D_d = -6$ eV and $D_u = 7.8$ eV are the dilation and uniaxial deformation potential constants respectively, and ε are

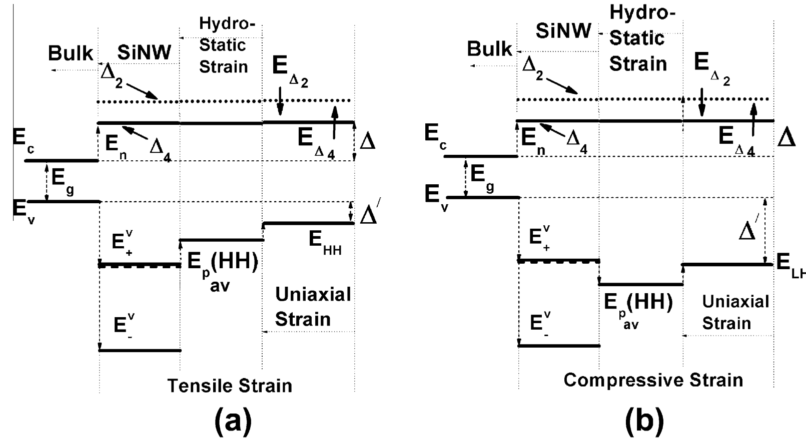

Fig. 6. Band alignment of the lowest conduction subband valleys at both Γ and off-Γ axes and valance subband using the degenerate perturbation theory under an application of a biaxial strain on [1 0 0] SiNW for (a) tensile and (b) compressive strain. The Δ_4 and Δ_2 subband valleys in relaxed SiNW are the results of difference in effective masses due to quantum confinement as arrested by sp^{3}d^{5}s* method. The average of the HH and LH subband (as shown by the horizontal dotted line below) E_+^v is assumed to coincide with the E_+^v for both the tensile and compressive cases due to higher effective mass of the former.

the isotropic strain component [10,24]. Using Eq. (20) the subband energies can then be written as

$$E_{\pm}^{\varepsilon}(k) = \frac{\hbar^2 k_{x_{min}}^2}{2m_{3_\pm}} + \frac{\hbar^2}{2m_{2_\pm}}\left(\frac{\pi}{d_y}\right)^2 + \frac{\hbar^2}{2m_{1_\pm}}\left(\frac{\pi}{d_z}\right)^2 \pm \left\{\delta E_c + \sqrt{\left(\frac{\hbar^2}{M_\pm}\left(\frac{\pi}{d_z}\right)\left(\frac{\pi}{d_y}\right)\right)^2}\right\} \quad (21)$$

In case of the valance subbands, the hydrostatic strain shifts the average energy of the nanowire valance band edge from E_+^v by an amount $E_{p_{av}}(HH) = a_v\left(\frac{2\varepsilon}{1-\nu}\right)$. This is further shifted to an amount $E_{HH} = -b_v\varepsilon\left(\frac{3\nu-1}{1-\nu}\right)$ in the presence of a uniaxial tensile strain as exhibited in Fig. 6a. In case of compressive strain, the $E_{p_{av}}(HH)$ is shifted to an amount $E_{LH} = 2b_v\varepsilon\left(\frac{3\nu-1}{1-\nu}\right)$ as shown in Fig. 6b in which a_v=2.46 eV and b_v = 2.35 eV are the valance band deformation potentials [22,25] and ν = 0.37 is the SiNW Poisson's ratio [26]. Thus, we see from the energy band diagram in Fig. 6a that the Γ axis direct band gap in a biaxially tensile strained [1 0 0] SiNW is given by

$$E_{g_{NW}}^{Direct}(\varepsilon > 0) = E_g + \Delta + \Delta'' \quad (22)$$

and the indirect energy band gap at off-Γ assumes the form

$$E_{g_{NW}}^{Indirect}(\varepsilon > 0) = E_g + \Delta' + \Delta'' \quad (23)$$

in which $\Delta = E_{1,1_-}^{\varepsilon}$, $\Delta' = E_{1,1_+}^{\varepsilon}$ and $\Delta'' = |E_+^v| - (E_{p_{av}} + E_{HH})$ where $E_{p_{av}}$ and E_{HH} are both positive quantities. Similarly for compressive strain, Eqs. (22) and (23) transforms as

$$E_{g_{NW}}^{Direct}(\varepsilon < 0) = E_g + \Delta + \Delta'' \quad (24)$$

and

$$E_{g_{NW}}^{Indirect}(\varepsilon < 0) = E_g + \Delta' + \Delta'' \quad (25)$$

for direct and indirect band gap respectively, where in this case $\Delta'' = |E_+^v| - (E_{p_{av}} + E_{LH})$ in which $E_{p_{av}}$ is negative while E_{LH} is positive quantity.

The effect of strain on the band gap in [1 0 0] SiNW has been exhibited in Fig. 7 for a 1.5 nm wire thickness. It appears that the rate of change of the direct and indirect band gap are different due to the difference in energy between $E_{1,1_-}^{\varepsilon}$, $E_{1,1_+}^{\varepsilon}$, $E_{p_{av}}$, E_{LH} and E_{HH} in both the regime of the strain. It should be noted that an increase in the tensile strain decreases the energy of the $E_{1,1_-}^{\varepsilon}$ subbands while the HH subbands shifts towards the valance band maxima position of the bulk Si. This marks a reduction of the band gap as the tensile strain increases. In case of uniaxial compressive strain, it is the $E_{1,1_-}^{\varepsilon}$ subband valley which shifts up together with LH, thus increasing the Γ axis band gap.

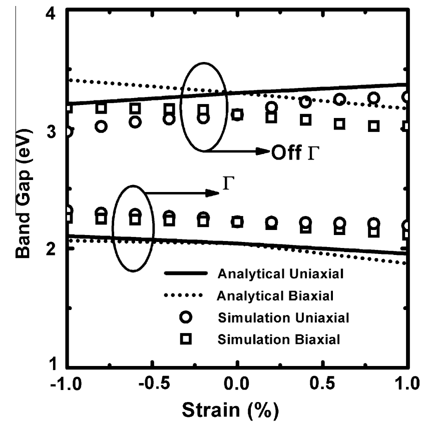

Fig. 7. Plot of the direct and indirect band gap as function of uniaxial and biaxial strain along [1 0 0] oriented SiNW. Symbols are the results of the ATK simulations.

Further, we see that the direct band gap increases as the uniaxial strain becomes more compressive. However the off-Γ band gap decreases with the increase in compressive strain. This remarkable effect leads to the crossing over of the two subband valleys in the very deep compressive strain zone. This essentially means that there occurs a direct to indirect band gap transition in the deep compressive zone and has also been exhibited numerically by Shiri et al. [7]. It should also be noted that with the increase in the cross-sectional dimension, the valley splitting difference between the lowest conduction subbands at Γ and off-Γ axis decreases. Thus, for higher dimensions, it appears that the transition from direct to indirect band gap should occur at relatively less compressive strain zone. However with the increase in the tensile strain the Γ axis band gap decreases while the off-Γ band gap increases. This shows that under uniaxial tensile strain, band gap remains direct always.

The scenario changes when the uniaxial strain is combined with the [0 0 1] hydrostatic strain. Under this biaxial strain condition, the band gap remains almost invariant with respect to strain at the Γ valley, while for the off-Γ valley it decreases when the strain

increases from compressive to tensile zone, and has been compared with the extracted sp^{3}d^{5}s* data.

The transport electron effective mass under the uniaxial strain can be written following Eq. (20) for Γ and off-Γ axis as

$$m_{x_-} = m_{1_-}\left(1 + \frac{\sqrt{\sigma_-}}{\sqrt{E_{g_{NW}}^{Direct}(\varepsilon) + \sigma_- - 2\phi_-^{\varepsilon}}}\right) \tag{26}$$

and

$$m_{x_+} = m_{1_+}\left(1 + \frac{\sqrt{\sigma_+}}{\sqrt{E_{g_{NW}}^{Indirect}(\varepsilon) + \sigma_+ - 2\phi_+^{\varepsilon}}}\right) \tag{27}$$

where $\phi_\pm^\varepsilon = \frac{\hbar^2}{2m_{2_\pm}}\left(\frac{\pi}{d_y}\right)^2 \pm \delta E_c$.

Using Eq. (26), the variation of the transport effective electron mass at the lowest energy subband in Γ axis as function of strain has been exhibited in Fig. 8. It appears from our analytical results that the transport effective mass in Γ valley is a very slowly varying function with strain within the ±1% zone which has also been predicted quite satisfactorily by Sajjad et al. [27] through sp^{3}d^{5}s* calculations.

2.6. Strained [1 1 0] SiNW

Using Eqs. (10) and (12) and including the off-diagonal shear strain term together with the uniaxial and biaxial strain, the appropriate strained electron energy dispersion relation can be extended following [10] as

$$\begin{aligned} E(K) = &\frac{\hbar^2(K_x+K_{x_{min}})^2}{2m_{1_4}} + \frac{\hbar^2}{2m_{2_4}}\left(\frac{\pi}{d_y}\right)^2 + \frac{\hbar^2}{2m_{3_4}}\left(\frac{\pi}{d_z}\right)^2 \\ &+ \frac{\hbar^2(K_x+K_{x_{min}})}{2m_{s_4}}\left(\frac{\pi}{d_y}\right) \\ &+ \left\{\delta E_c + \sqrt{\left(\frac{\hbar^2 k_0}{m_{3_+}}\left(\frac{\pi}{d_z}\right)\right)^2 + \left(D\varepsilon_{xy} - \frac{\hbar^2}{2M_4}\left((K_x+K_{x_{min}})^2 - \left(\frac{\pi}{d_y}\right)^2\right)\right)^2}\right\} \end{aligned} \tag{28}$$

for off-Γ valley and

$$\begin{aligned} E(K) = &\frac{\hbar^2(K_x+K_{x_{min}})^2}{2m_{1_2}} + \frac{\hbar^2}{2m_{2_2}}\left(\frac{\pi}{d_y}\right)^2 + \frac{\hbar^2}{2m_{3_2}}\left(\frac{\pi}{d_z}\right)^2 \\ &- \left\{\delta E_c + \sqrt{\left(\frac{\hbar^2 k_0}{m_{3_-}}\left(\frac{\pi}{d_z}\right)\right)^2 + \left(D\varepsilon_{xy} - \frac{\hbar^2}{2M_2}\left((K_x+K_{x_{min}})^2 - \left(\frac{\pi}{d_y}\right)^2\right)\right)^2}\right\} \end{aligned} \tag{29}$$

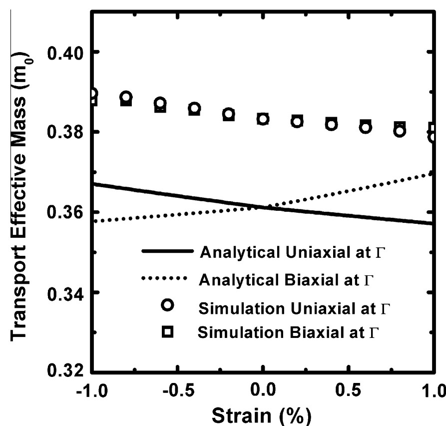

Fig. 8. Plot of the transport effective electron mass as function of uniaxial and biaxial strain at Γ valley. The symbol represents the extracted data from the energy band structure obtained using ATK simulation.

for Γ valley in which D = 14 eV is the shear strain deformation potential [10].

Using Eqs. (28) and (29), the subband energies can then respectively be written as

$$\begin{aligned} E_{1,1_4}^{\varepsilon} = &\frac{\hbar^2 K_{x_{min}}^2}{2m_{1_4}} + \frac{\hbar^2}{2m_{2_4}}\left(\frac{\pi}{d_y}\right)^2 + \frac{\hbar^2}{2m_{3_4}}\left(\frac{\pi}{d_z}\right)^2 + \frac{\hbar^2 K_{x_{min}}}{2m_{s_4}}\left(\frac{\pi}{d_y}\right) \\ &+ \left\{\delta E_c + \sqrt{\left(\frac{\hbar^2 k_0}{m_{3_+}}\left(\frac{\pi}{d_z}\right)\right)^2 + \left(D\varepsilon_{xy} - \frac{\hbar^2}{2M_4}\left(K_{x_{min}}^2 - \left(\frac{\pi}{d_y}\right)^2\right)\right)^2}\right\} \end{aligned} \tag{30}$$

and

$$\begin{aligned} E_{1,1_2}^{\varepsilon} = &\frac{\hbar^2}{2m_{2_2}}\left(\frac{\pi}{d_y}\right)^2 + \frac{\hbar^2}{2m_{3_2}}\left(\frac{\pi}{d_z}\right)^2 \\ &- \left\{\delta E_c + \sqrt{\left(\frac{\hbar^2 k_0}{m_{3_-}}\left(\frac{\pi}{d_z}\right)\right)^2 + \left(D\varepsilon_{xy} - \frac{\hbar^2}{2M_2}\left(\frac{\pi}{d_y}\right)^2\right)^2}\right\} \end{aligned} \tag{31}$$

In case of the valance subbands, the hydrostatic strain shifts the average energy of the nanowire valance band edge from E_+^v by an amount $E_{p_{av}}(HH) = 2a_v\varepsilon\left(\frac{1-2v}{1-v}\right)$. This is further shifted to an amount $E_{LH} = -2b_v\varepsilon\left(\frac{1+v}{1-v}\right)$ in the presence of a uniaxial tensile strain as exhibited in Fig. 9a. In case of compressive strain, the $E_{p_{av}}(HH)$ is shifted to an amount $E_{HH} = b_v\varepsilon\left(\frac{1+v}{1-v}\right)$ as shown in Fig. 9b. This is in opposite to what has been observed in case of $\langle 100\rangle$ uniaxial tensile strain. Thus, we see from Eqs. (15) and (31) that the Γ axis direct band gap in a biaxially tensile strained [1 1 0] SiNW is given by

$$E_{g_{NW}}^{Direct}(\varepsilon > 0) = E_g + \Delta + \Delta'' \tag{32}$$

while from Eqs. (15) and (30), the indirect energy band gap at off-Γ has the form

$$E_{g_{NW}}^{Indirect}(\varepsilon > 0) = E_g + \Delta' + \Delta'' \tag{33}$$

in which $\Delta = E_{1,1_2}^{\varepsilon}$, $\Delta' = E_{1,1_4}^{\varepsilon}$ and $\Delta'' = |E_+^v| - (E_{p_{av}} + E_{LH})$ where $E_{p_{av}}$ and E_{LH} are both positive quantities.

In case of compressive strain, Eqs. (32) and (33) transforms as

$$E_{g_{NW}}^{Direct}(\varepsilon < 0) = E_g + \Delta + \Delta'' \tag{34}$$

and

$$E_{g_{NW}}^{Indirect}(\varepsilon < 0) = E_g + \Delta' + \Delta'' \tag{35}$$

for direct and indirect band gap respectively, where $\Delta'' = |E_+^v| - (E_{p_{av}} + E_{HH})$, in which $E_{p_{av}}$ is negative while E_{HH} is positive quantity.

Fig. 10 exhibits the dependency of the band gap on the strain for a 1.5 nm wire thickness. We see that in this case there also exits crossing over of the two subband valleys in a very high compressive strain zone for both uniaxial and biaxial conditions as also arrested by others numerically [7].

It should be noted that the transport electron effective mass is independent of the uniaxial and biaxial strain in [1 1 0] oriented SiNW [28]. Using Eqs. (28) and (29), we find analytically that the transport electron effective mass under the presence of shear strain in Γ and off-Γ axis to be

$$\begin{aligned} m_{x_2}(\varepsilon) = m_{1_2}\Bigg\{1 + &\frac{m_{1_2}}{M_2}\left(D\varepsilon_{xy} + \frac{\hbar^2}{2M_2}\left(\frac{\pi}{d_y}\right)^2\right) \\ &\times \left[\left(\frac{\hbar^2 k_0}{m_{3_-}}\left(\frac{\pi}{d_z}\right)\right)^2 + \left(D\varepsilon_{xy} + \frac{\hbar^2}{2M_2}\left(\frac{\pi}{d_y}\right)^2\right)^2\right]^{-\frac{1}{2}}\Bigg\}^{-1} \end{aligned} \tag{36}$$

and

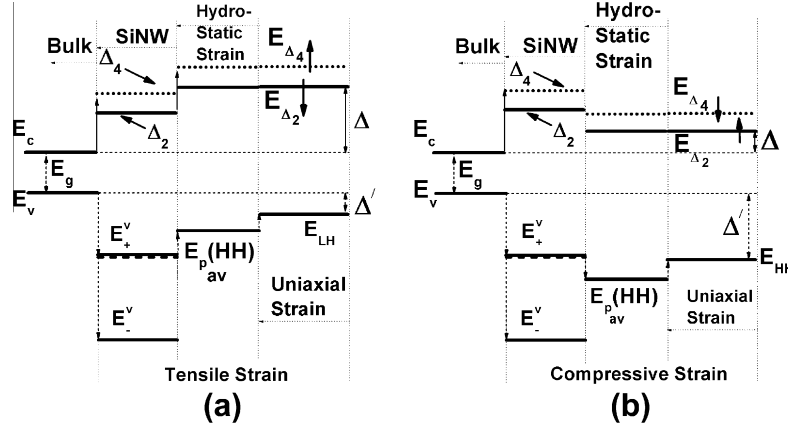

Fig. 9. Band alignment of the lowest conduction subband valleys at both Γ and off-Γ axes and valance subband using the degenerate perturbation theory under an application of a biaxial strain on [1 1 0] SiNW for (a) tensile and (b) compressive strain. The Δ_2 and Δ_4 subband valleys in relaxed SiNW are the results of difference in effective masses due to quantum confinement as arrested by sp^{3}d^{5}s* method. The average of the HH and LH subband (as shown by the horizontal dotted line below) E_+^v is assumed to coincide with the E_+^v for both the tensile and compressive cases due to higher effective mass of the former.

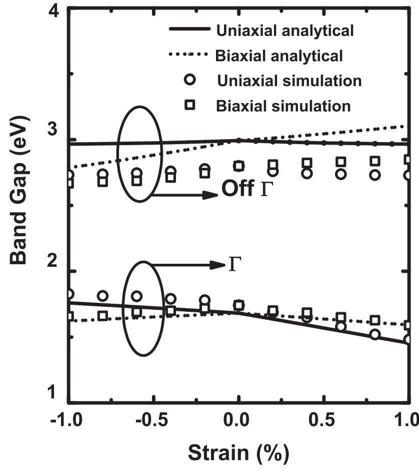

Fig. 10. Plot of the direct and indirect band gap as function of uniaxial and biaxial strain along [1 1 0] oriented SiNW. Symbols are the results of the ATK simulations.

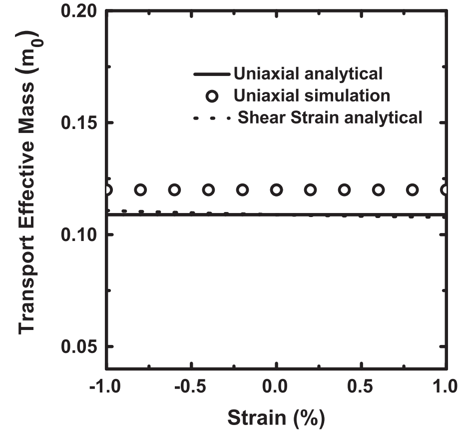

Fig. 11. Plot of the transport effective electron mass as function of uniaxial along [1 1 0] and shear strain at Γ valley. The effect of biaxial strain coincides with the uniaxial one. The symbol represents the extracted data from the energy band structure obtained using ATK simulation.

$$m_{x_4}(\varepsilon) = m_{1_4}\left\{1 + \frac{m_{1_4}}{M_4}\xi(\varepsilon)\right\}^{-1} \tag{37}$$

respectively in which

$$\xi = \frac{1}{\sqrt{\zeta(\varepsilon)}}\left\{D\varepsilon_{xy} + \frac{\hbar^2}{2M_4}\left[3K_{x_{min}}^2 - \left(\frac{\pi}{d_y}\right)^2\right] - \frac{2}{\zeta(\varepsilon)}\left(\frac{\hbar^2 K_{x_{min}}}{2M_4}\right)^2 \times \left[D\varepsilon_{xy} + \frac{\hbar^2}{2M_4}\left(K_{x_{min}}^2 - \left(\frac{\pi}{d_y}\right)^2\right)\right]^2\right\}$$

and

$$\zeta(\varepsilon) = \left[\left(\frac{\hbar^2 k_0}{m_{3_+}}\left(\frac{\pi}{d_z}\right)\right)^2 + \left[D\varepsilon_{xy} + \frac{\hbar^2}{2M_4}\left(K_{x_{min}}^2 - \left(\frac{\pi}{d_y}\right)^2\right)\right]^2\right].$$

Using Eq. (36), the variation of the transport effective electron mass at the lowest energy subband in Γ axis as function of shear strain has been exhibited in Fig. 11. The effects of uniaxial and biaxial strain have also been exhibited in the same figure which produces no change in the effective mass. We could not exhibit the sp^{3}d^{5}s* variation of the effective mass in both the channel oriented direction due to the questionable accuracy of applying the numerical tight binding model [29]. Our analytical model may find useful in predicting the effective mass when more accurate simulation technique is available.

2.7. Mobility

It should be noted that the main focus of the present work deals with the effective mass and energy band gap of relaxed and strained SiNW along different crystal orientations and cross-sections. However, we have discussed below the SiNW electron mobility when varied with respect to cross-section and strain (Fig. 12) by using a simple intra-subband acoustic-phonon scattering formalism as $\mu = \frac{e}{k_B T}\sqrt{\frac{2k_B T}{\pi m^*}}\frac{8d^2\hbar^2\rho v_s^2}{9m^* D_A^2}$, where k_B the Boltzmann's constant, T(= 300 K) the temperature, m^* the effective mass at the respective valleys, ρ(=2.329 × 10^3 kg m^{-3}) the Si mass density, v_s the sound velocity (= 8.4 × 10^3 ms^{-1} and 5.86 × 10^3 ms^{-1} along [1 0 0] and [1 1 0] direction respectively) and D_A(= 12 eV) is the acoustic phonon scattering potential [30]. The mobility model in this manuscript realises from only fact of the change of effective mass under both relaxed and strained conditions. From Fig. 12a, it appears that this mobility model exhibits a square-law variation

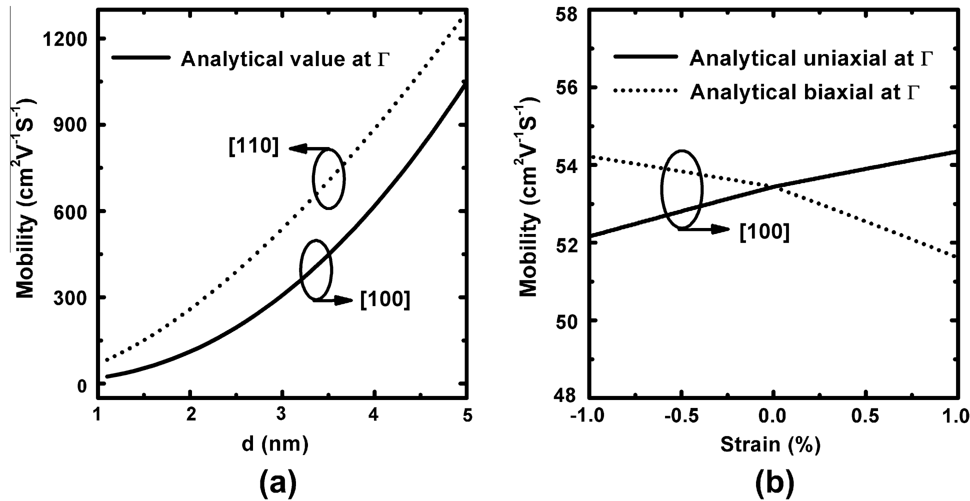

Fig. 12. Plot of the electron mobility for (a) relaxed and (b) strained SiNW.

with the cross-sectional dimension. Fig. 12b shows the variation of this mobility with strain. In case of [1 1 0] SiNW, the effective mass at the Γ valley remains unchanged with both uniaxial and biaxial strain which makes this mobility to be constant with strain. However for [1 0 0] direction, increasing uniaxial and biaxial tensile strain has opposite variation on the mobility. As, it is understood now that the main effect of increase of the electron mobility under strained SiNW is due to the suppression of the intervalley phonon (g-type and f-type) and surface roughness scattering mechanisms [31], the detailed calculation of which perhaps will not result a closed form solution that we intend to do in this work. However as this model does not incorporate the convergence of discrete model (nanowire within 1–4 nm square cross-sectional dimension) to its corresponding continuum model (above 4 nm cross-sectional dimension), we have not shown its corresponding convergence for 4 nm and beyond for [1 1 0] and [1 0 0] orientation. But the mobility model that we have given in this manuscript may of course give a hint to the corresponding trends in both relaxed and strained SiNW.

The results and the methodologies as carried out in this work can be tuned further by modifying the nanowire dispersion relation by considering the valley splitting for the description of the electron mobility and electrical resistance through the intra subband transition. In addition for our present case, we did not consider the tensile and compressive strain beyond ±1% because of the fracture issues in the strain induced silicon process technology [32]. Besides, the inclusion of the spin orbit interaction and plane wave function due to the Hydrogen passivation would certainly increase the accuracy of our analytical results, although the qualitative features of the band gap and the effective masses both in relaxed and strained case would not change.

Finally, we wish to state that the methods as presented in this work for the formalism of both the direct and indirect band gap and the transport electron effective mass in the presence of strain may also be useful in the determination of different band structure dependent electronic transport properties in uniaxial ([1 1 1] direction) and biaxially ([1 1 1] and [0 0 1]) strained [1 1 1] channel oriented SiNWs.

3. Conclusions

In this paper, we present an analytical technique to quantify the direct and indirect energy band gap and transport electron effective mass in a [1 0 0] and [1 1 0] oriented relaxed and strained SiNW. Using a degenerate perturbation theory, we investigate the effect of the spatial, uniaxial and biaxial and shear strain on these parameters. The analytical results of our proposed model for both relaxed and strained SiNWs are in good agreement with the existing numerical models and with that of our corresponding data extracted from the nearest neighbour empirical tight binding sp^{3}d^{5}s* method. Further, the positions of the conduction subband valleys under the presence of strain are in accordance with the simulation results exhibited elsewhere.

Acknowledgment

This work was supported by Indian Institute of Science and Indian Space Research Organization, Space Technology Cell, India under Grant No. ISTC/EED/SM/253.

References

[1] Baykan MO, Thompson SE, Nishida T. Strain effect on three dimensional, two dimensional, and one dimensional silicon logic devices: predicting the future of strained silicon. J Appl Phys 2010;108(9):093716.
[2] Neophytou N, Paul A, Lundstrom MS, Klimeck G. Bandstructure effects in silicon nanowire electron transport. IEEE Trans Electron Dev 2008;55(3):1286.
[3] Yan JA, Yang L, Chou MY. Size and orientation dependence in the electronic properties of silicon nanowires. Phys Rev B 2007;76:115319.
[4] Wang J, Rahman A, Ghosh A, Klimeck G, Lundstrom MS. On the validity of the parabolic effective-mass approximation for the IV calculation of silicon nanowire transistors. IEEE Trans Electron Dev 2005;52(7):1589–95.
[5] Zheng E, Rivas C, Lake R, Alam K, Boykin TB, Klimeck G. Electronic properties of silicon nanowires. IEEE Trans Electron Dev 2005;52(6):1003–97.
[6] Uchida K, Kinoshita A, Saitoh M. Carrier transport in (1 1 0) nMOSFETs: subband structures, non-parabolicity, mobility characteristics, and uniaxial stress engineering. In: IEEE international electron devices meeting (IEDM, 2006), vol. 1; 2006.
[7] Shiri D, Kong Y, Buin A, Anantram MP. Strain induced change of bandgap and effective mass in silicon nanowires. Appl Phys Lett 2008;93:073114.
[8] International Technology Roadmap for Semiconductors; 2009 <http://www.itrs.net/Links/2009ITRS/2009Chapters2009Tables/2009ERD.pdf>.
[9] Atomistix ToolKit (ATK), QuantumWise simulator <http://www.quantumwise.com/>.
[10] Sverdlov V. Strain-induced effects in advanced MOSFETs. Springer; 2011.
[11] Sverdlov V, Kosina H, Selberherr S. Electron subband dispersions in ultra-thin silicon films from a two-band **k.p** theory. J Comput Electron 2008;7(3):164–7.
[12] Dresselhaus G, Kip AF, Kittel C. Cyclotron resonance of electrons and holes in silicon and germanium crystals. Phys Rev 1955;98:368–84.
[13] Sajjad RN, Alam K, Khosru QDM. Parametrization of a silicon nanowire effective mass model from sp^{3}d^{5}s* orbital basis calculations. Semicond Sci Technol 2009;24:045023.
[14] Windbacher T, Sverdlov V, Baumgartner O, Selberherr S. Electron subband structure in strained silicon UTB films from the Hensel–Hasegawa–Nakayama model – part 1 analytical consideration and strain-induced valley splitting. Solid State Electron 2010;54:137142.

[15] Nag BR. Electron transport in compound semiconductors. Springer-Verlag; 1980.
[16] Lundstrom MW. Fundamentals of carrier transport. Cambridge University Press; 2000.
[17] Zhao X, Wei CM, Yang L, Chou MY. Quantum confinement and electronic properties of silicon nanowires. Phys Rev Lett 2004;92. 236805(1)-(4).
[18] Yeh CY, Zhang SB, Zunger A. Confinement, surface, and chemisorption effects on the optical properties of Si quantum wires. Phys Rev B 1994;50: 1440514415.
[19] Dhar S, Ungersbock E, Kosina H, Grasser T, Selberherr S. Electron mobility model for ⟨1 1 0⟩ stressed silicon including strain-dependent mass. IEEE Trans Electron Dev 2007;6:97–100.
[20] Sajjad RN, Bhowmick S, Khosru Q. Cross-sectional shape effects on the electronic properties of silicon nanowires. In: IEEE international conference on electron devices and solid-state circuits (EDSSC); 2008. p. 1–4.
[21] De Walle CGV, Martin RM. Theoretical calculations of heterojunction discontinuities in Si/Ge systems. Phys Rev B 1986;34:5621–34.
[22] Hensel JC, Feher G. Cyclotron resonance experiments in uniaxially stressed silicon: valence band inverse mass parameters and deformation potentials. Phys Rev 1963;129:10411062.
[23] Hong KH, Kim J, Lee SH, Shin JK. Strain-driven electronic band structure modulation of Si nanowires. Nano Lett 2008;8(5):1335–40.
[24] Sun Y, Thompson SE, Nishida T. Strain effect in semiconductors: theory and device applications. Springer; 2010.
[25] Yu PY, Cardona M. Fundamentals of semiconductors: physics and materials properties. Springer; 2010.
[26] Durandurdu M. Ab initio modeling of small diameter silicon nanowires. Phys Stat Sol (b) 2006;243:R7–9.
[27] Sajjad RN, Alam K. Electronic properties of a strained ⟨1 0 0⟩ silicon nanowire. J Appl Phys 2009;105(4):044307.
[28] Maegawa T, Yamauchi T, Hara T, Tsuchiya H, Ogawa M. Strain effects on electronic bandstructures in nanoscaled silicon: from bulk to nanowire. IEEE Trans Electron Dev 2009;56(4):553.
[29] Boykin TB, Luisier M, Jelodar MS, Klimeck G. Strain-induced, off-diagonal, same-atom parameters in empirical tight-binding theory suitable for [1 1 0] uniaxial strain applied to a silicon parametrization. Phys Rev B 2010;81: 125202.
[30] Yamada Y, Tsuchiya H, Ogawa M. Atomistic modeling of electron–phonon interaction and electron mobility in Si nanowires. J Appl Phys 2012;111: 063720.
[31] Liang R, Li D, Xu J. A universal electron mobility model of strained Si MOSFETs based on variational wave functions. Solid State Electron 2008;52:863870.
[32] Maiti CK, Chattopadhyay S, Bera LK. Strained-Si heterostructure field effect devices. Taylor Francis; 2007.